Nanoscale

Accepted Manuscript

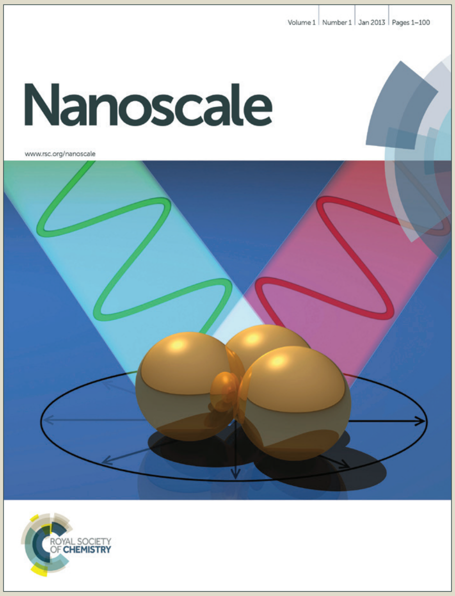

ROYAL SOCIETY
OF **CHEMISTRY**

www.rsc.org/nanoscale

Journal Name

RSCPublishing

ARTICLE

Confined growth of Carbon Nanoforms in one-dimension by fusion of anthracene rings inside the pores of MCM-41

Cite this: DOI: 10.1039/x0xx00000x

Received 00th January 2012,
Accepted 00th January 2012

DOI: 10.1039/x0xx00000x

www.rsc.org/

Concha Bosch-Navarro[a], Eugenio Coronado[a,]*, Carlos Martí-Gastaldo[a,]†,* Pedro Amorós[b]

We report a simple two-step procedure that uses anthracene, a cheap polyaromatic hydrocarbon with low melting point, as molecular precursor to produce carbon nanoforms (CNFs). First, we describe the chemical synthesis of graphite from the fusion of anthracene rings at relatively low temperature (520ºC) followed by cyclodehydrogenation. Next, we extend this protocol to the synthesis of CNFs by confining the molecular precursor in a mesoporous host like MCM-41. The confined environment favors one-dimensional growth of CNFs with sizes controlled by the pores of the mesoporous host.

INTRODUCTION

Research on graphene (G) has generated enormous excitement because of its fascinating physical properties and their potential impact in technological applications.[1-3] Multiple approaches of different nature have been developed to produce G over the past few years. Concerning "top-down" methodologies, chemical reduction of graphite oxide (GO)[4] and micromechanical cleavage or liquid-phase exfoliation of graphite are arguably the most common.[6] Whilst the first enables production of G with good yields, its electronic properties are compromised due to the introduction of defects to the sp^2 electronic structure of pristine G.[5] The exfoliation route enables production of high-quality G but in very low yields and with sizes limited to micrometers. In contrast, the "bottom-up" approach permits producing high-quality G while controlling the dimensionality of the resulting carbon nanoforms. In this context, chemical vapor deposition (CVD)[7] or organic synthesis of G from reaction of small aromatic hydrocarbons,[8] are worth-mentioning. CVD is probably the most promising technique nowadays, but it requires high temperatures and pressures which translates into a very expensive and technologically demanding process that generally leads to variable yields.[9] Recent works have also revealed that the quality of the G sheets are compromised during the early stage of the CVD process by the formation of defective pentagons, which degrade the quality of the carbon layers and disrupt their electronic properties.[10] This limitation might be overcome by tailoring G growth from direct reaction of small aromatic hydrocarbons containing only six-membered rings. Still, this synthetic route usually involves very complicated procedures based on complex organic reactions.[11-12] Hence, developing new and easier strategies to obtain tailor-made G is highly desirable. To this end, the use of appropriated precursors is essential. Previous reports illustrate the efficiency of polyaromatic hydrocarbons (PAHs) to drive the growth of G by cyclodehydrogenation of the sublimated precursors catalyzed by a variety of metallic substrates[12-14] or the use of other organic precursors to produce graphitic nanoforms by chemical confinement.[15-16] Still, the identification of alternative precursors that enable the formation of graphene without the aid of a catalyst is highly desirable as it would allow using non-metallic substrates or even producing bulk G without an assisting substrate, thus reducing the production costs.

In this context, Talyzin *et al.* have recently reported the synthesis of G from reaction of coronene (*cor*) molecules confined into a nanometric scaffold.[17,18] Here we propose the use of anthracene (*anth*) - a substantially cheaper PAH - as a suitable precursor for the synthesis of G (SI1). The high melting point of *cor* (438 ºC) translates into a high kinetic energy that limits the fusion of carbon oligomers instead.[17] This energy barrier is lower for *anth* (*c.f.* 218 ºC), thus favoring the formation of extended carbon layers from these molecular precursors. Even more, its lower boiling point (340 ºC) makes it more versatile as it facilitates its sublimation and further deposition over substrates or confinement into solid-state hosts.[18,19] Subjected to suitable thermal treatment, any of these last routes might lead to the formation of G of superior physical quality than that enabled by non-assisted fusion of PAHs. To date, this strategy has allowed for the synthesis of graphene nanoribbons (GNRs) by using CNTs as templates.[18,20-21] However, the use of mesoporous hosts in this context remains relatively unexplored.[22] MCM-41 offers a scaffold with uniform mesopores that range from 2 to 10 nm depending on the surfactant employed in the synthesis.[22] Besides its use as catalytic matrix, support for drug delivery or absorbent, its ability to intercalate molecular species has been exploited to encapsulate different nanoparticles or single molecule

Journal Name RSCPublishing

ARTICLE

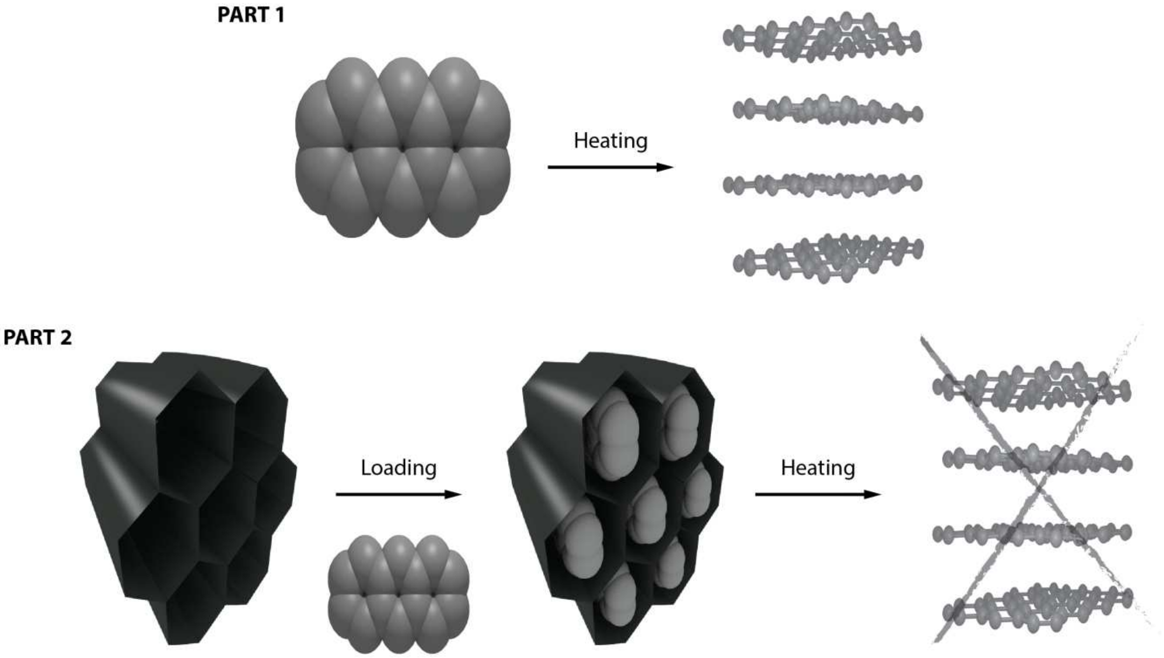

Scheme 1. Scheme illustrating the synthesis of graphite (top) and CNFs (bottom) from anthracene. Part 1: graphite is obtained by the thermal fusion of free anthracene molecules. Part 2: confinement of anthracene into the pores of mesoporous MCM-41 prevents π-π stacking between neighboring anth molecules upon fusion driving the formation of 1D CNFs rather than bulk 3D graphite.

magnets,[23] or even to grow carbon nanowire arrays.[24-26] Still, the intercalation of PAH guests to explore the formation of CNFs inside the host's pores has not been explored yet. MCM-41 is an ideal candidate to direct the growth of these species by suitable thermal treatment of confined PAH molecules since it offers a 2D regular distribution of pores, high thermal stability and can be easily removed from the carbon product by etching with hydrofluoric acid. The use of *anth* over other candidates bearing a bigger number of aromatic rings like *cor* is also recommendable as this increases the hydrophobicity of the guest, thus hindering the filling of the pores of MCM-41.[27]

We report the formation of graphite from thermally driven fusion of anth without the aid of a catalyst (Scheme 1, Part 1). This PAH precursor also enables preferential formation of one-dimensional CNFs along the pores of MCM-41. Our results also reveal that their size is controlled by the porosity metrics of the host and the crystallinity of the resulting carbon is increased by the spatial confinement of th**e molecules (Scheme 1, Part 2).**

RESULTS AND DISCUSSION

Synthesis of graphite from anthracene. Graphite was obtained by direct fusion of *anth* rings following a two-step procedure (Fig.1a). First, *anth* was loaded inside a quartz ampoule and sealed under vacuum. The system was then stepwise heated up to 520ºC as described in SI9. The gradients of temperature used were chosen on the basis of the melting point of *anth* (218 ºC). As reported for the thermal reaction of related PAHs,[17] in the first stage from 20 to 320ºC, the aromatic rings start to fuse giving rise to low-dimensional carbon oligomers (G1). As the system grows in size, its melting point and decomposition temperature increases so the temperature was ramped up to 420 and 520 ºC in two consecutive steps. This was followed by an annealing in N_2 over 24 hours. This treatment favors the cyclodehydrogenation reaction that drives the formation of C-C bonds necessary to form graphite (G2).[14]

Color evolution is a useful tool to monitor the formation of more extended carbon species as result of the increasing conjugation.[28] We observe how the original white colour of anth evolves into brown for G1 and finally becomes black for G2 (Fig.1b).

Infra Red Spectroscopy (FT-IR). *Anth* and G1 show almost equivalent FT-IR spectra (SI2) with a peak centered at 3047 cm^{-1} corresponding to the stretching of aromatic C-H bonds, and numerous signals between 1300 and 1600 cm^{-1} (annular backbone) and in the 950-1250 cm^{-1} interval (breathing modes of the in-plane aromatic C-H vibrations). They also display two intense signals at 736 cm^{-1} and 883 cm^{-1} from the breathing modes of the out-of-plane aromatic C-H vibrations. Albeit *anth* and G1 display almost

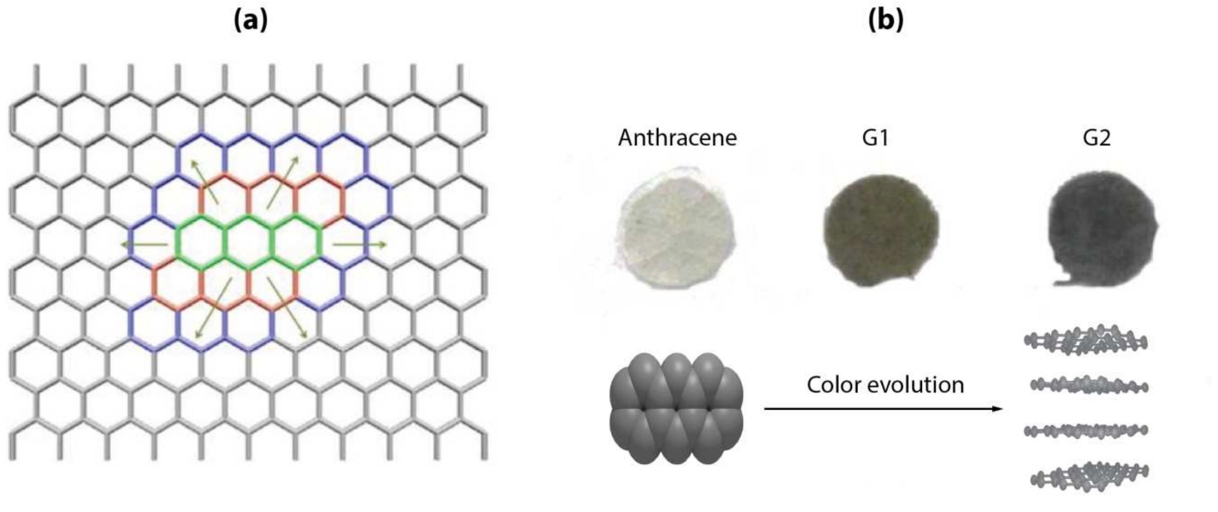

Figure 1. a) Schematic illustration of the growth of a 2D graphene flake from anthracene. Graphene layers would give rise to 3D graphite from π-π stacking between neighboring layers. b) Experimental color evolution of the thermal conversion of anthracene (in white) into G2 (black). Picture taken from powdered samples diluted in KBr.

equivalent IR features, HR-TEM and Raman spectroscopy reveal important morphological and structural differences (*vide infra*). This is likely due to the presence of non-reacted *anth* in G1, as confirmed with X-ray Powder Diffraction (XRPD) and Thermogravimetric Analysis (TGA). *Anth* is more active in the IR and dominates the spectrum of G1, preventing the observation of new bands. In contrast, the spectrum of G2 shows important changes. The signals from *anth* almost disappear upon annealing and only the intense bands linked to the out-of-plane aromatic C-H vibrations remain, suggesting that these groups must be present in G2, probably at the new graphitic sheet rims. G2 also displays the presence of two new bands at 1550 and 1130 cm^{-1} that correspond to ν(C=C) and δ(C=C) groups and support the formation of a graphitic-type structure.[29]

X-Ray powder diffraction (XRPD). Fig.2a shows the XRPD of *anth*, G1, G2 and commercially available graphite. G1 is poorly crystalline and its XRPD is dominated by a broad peak between 10-24º and the presence of the (001) and (100) diffraction lines that correspond to non-reacted *anth*. All these features vanish in G2 that only displays an intense peak centered at 25.8º (3.45 Å), in agreement with the position of (001) in graphite (d_{001}=3.36 Å). This must result from the packing in the solid-state of the G layers that result from the fusion and cyclodehydrogenation of the *anth* PAHs. In absence of an auxiliary template, the intermolecular π-π interactions operating between anth molecules will favor a 3D packing, thus yielding a multi-layered arrangement once the fusion has taken place.[20] As described later, this control over the dimensionality exerted by supramolecular interactions can be avoided by confining the PAHs in the nanometric cavities of a host before thermal reaction.

Thermogravimetric Analysis (TGA). The process of graphitization was further analyzed in terms of increased thermal stability. As shown in Fig.2b, *anth* decomposes at very low temperature (230 ºC). G1 displays a first weigh loss at 230 ºC (5%), which agrees with the presence of unreacted *anth*, whilst the pyrolysis of 95% of the remaining sample occurs at much higher temperatures (655 ºC). The thermal stability of G2 is very similar to G1 (630ºC), although the pyrolysis is more abrupt and consistent with a more homogeneous material. Still, G2 is not as stable as pristine graphite (741ºC), probably due to the presence of defects in the carbon layers intrinsic to the synthetic route as confirmed below with μ-Raman spectroscopy.

Raman Spectroscopy. As shown in Fig.3, the spectrum of *anth* displaying multiple peaks is quite different from G1 and G2. These last display a clear evolution towards a graphitic-type Raman response characterized by the presence of G and D bands at 1580 and 1340 cm^{-1}, respectively. The G band corresponds to E_{2g} vibrational modes characteristic of highly conjugated sp^2 systems, whilst the D band is connected to the reduction of the sp^2 domains. The intensity of D is proportional to the presence of defects and is generally weak for defect-free graphitic materials.[30] Whilst the G-bands can be clearly observed for G1 and G2, D splits into 4 peaks in G1 suggesting the presence of carbon oligomers.[931] G2 displays a single G-band but blue-shifted (1595 vs. 1580 cm^{-1}) and significantly broader than graphite, confirming the presence of sp^3 defects across the carbon layers as already pointed out by the TGA study.[32] The down-shift affecting the G band when going from G1 to G2 (1610 cm^{-1} vs 1595 cm^{-1}) confirms that the thermal annealing favors the formation of less defective graphite.

High Resolution Electron Microscopy (HR-TEM). HR-TEM images were acquired from freshly prepared dispersions of G1 and G2 in N-methylpirrolidone (NMP) dropped over a carbon-coated copper grid. G1 can be described as very defective carbon layers featuring a big number of holes across the surface (Fig.4). For contrast, annealing of G1 yields bigger, denser layers in G2 (Fig.4), with morphologies comparable to graphite. The arrow in Fig.4 highlights the aggregation of at least 5-layers in G2, confirming its graphitic-type structure. Unfortunately, the poor crystallinity of the formed layers (see XRPD above) limited the collection of the hexagonal diffraction pattern by Selected Area Electron Diffraction (SAED) characteristic of graphene layers.

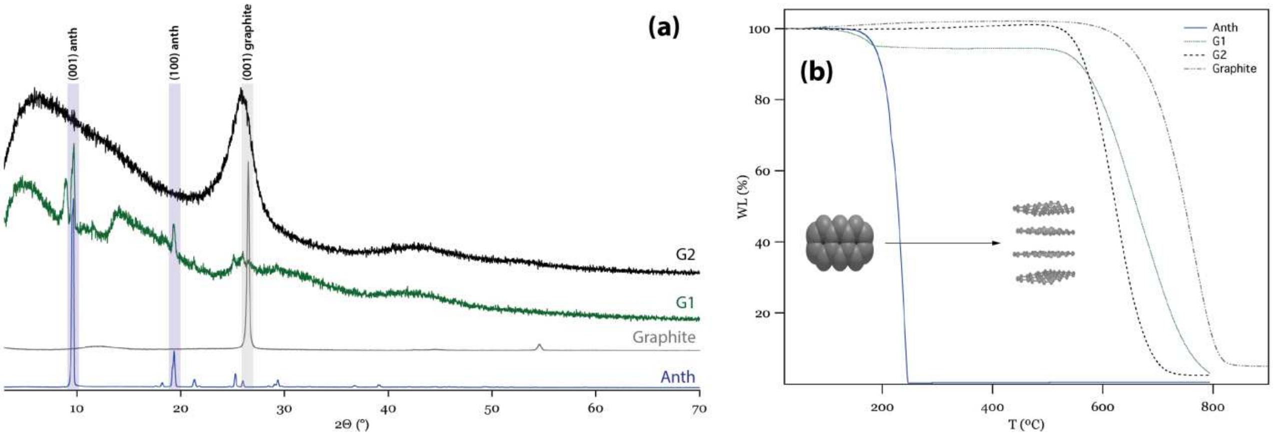

Figure 2. (a) XRPD of anthracene (blue), graphite (grey), G1 (green) and G2 (black). Blue and grey stripes highlight the most representative diffraction features of anth and graphite present in G1 and G2, respectively. (b) Thermogravimetry in air of anth (blue), graphite (grey), G1 (green) and G2 (black) showing the increasing thermal stability of G1 and G2 over anth.

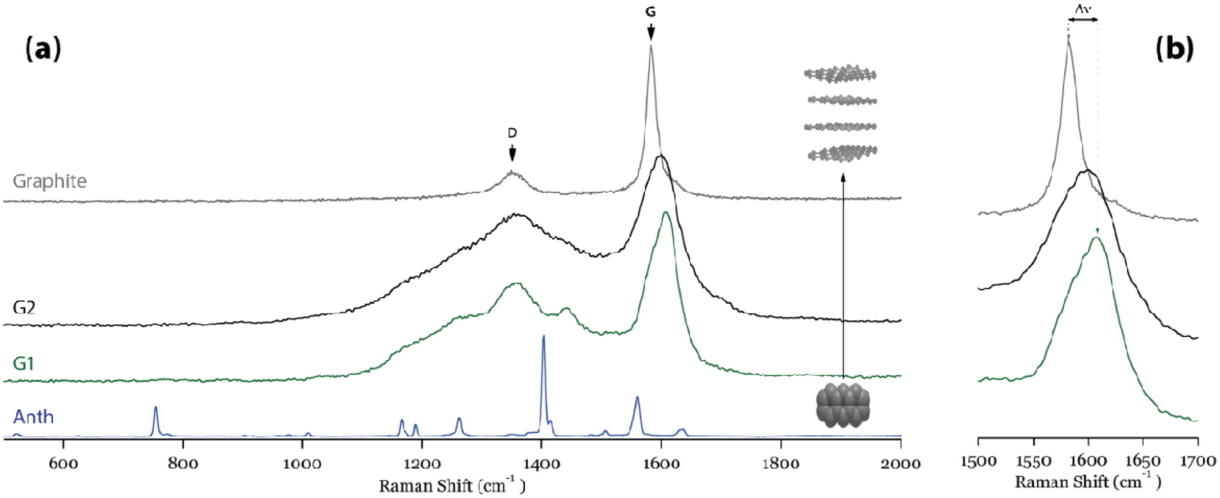

Figure 3. (a) Raman spectra of anthracene (blue), G1 (green), G2 (black) and graphite (grey). (b) Zoom-in area highlighting the blue-shift of the G band in G1 and G2 with respect to graphite.

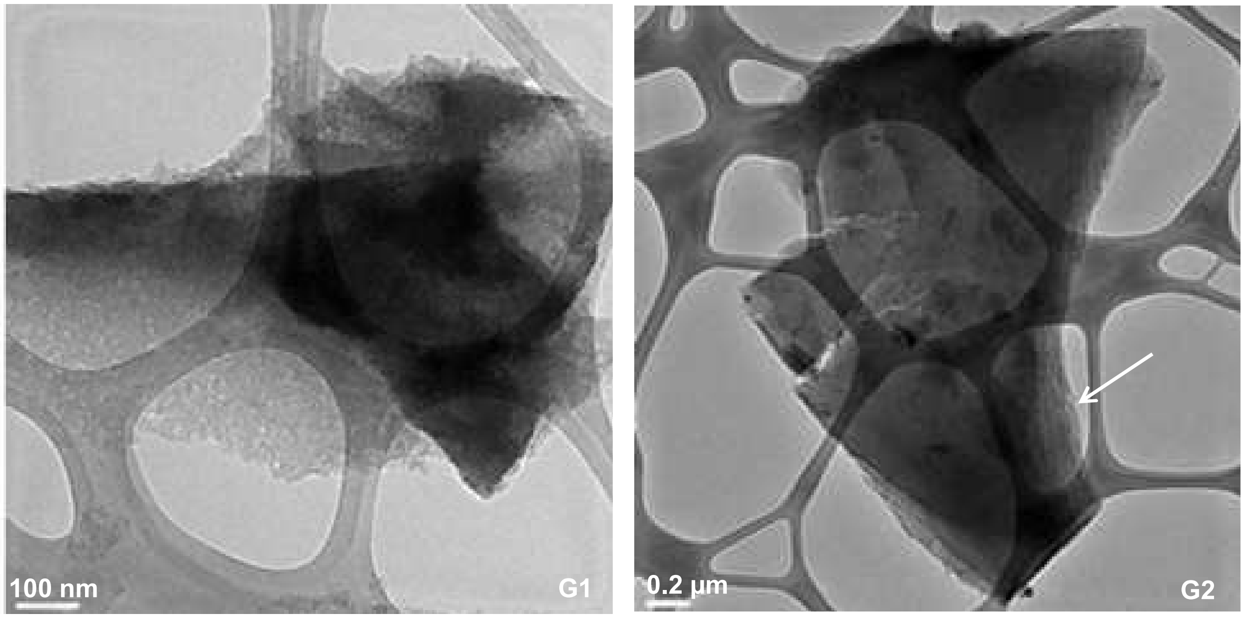

Figure 4. HR-TEM images of G1 (*left*) and G2 (*right*). An arrow highlights the area that displays more clearly steps corresponding to the aggregation of carbon layers in G2.

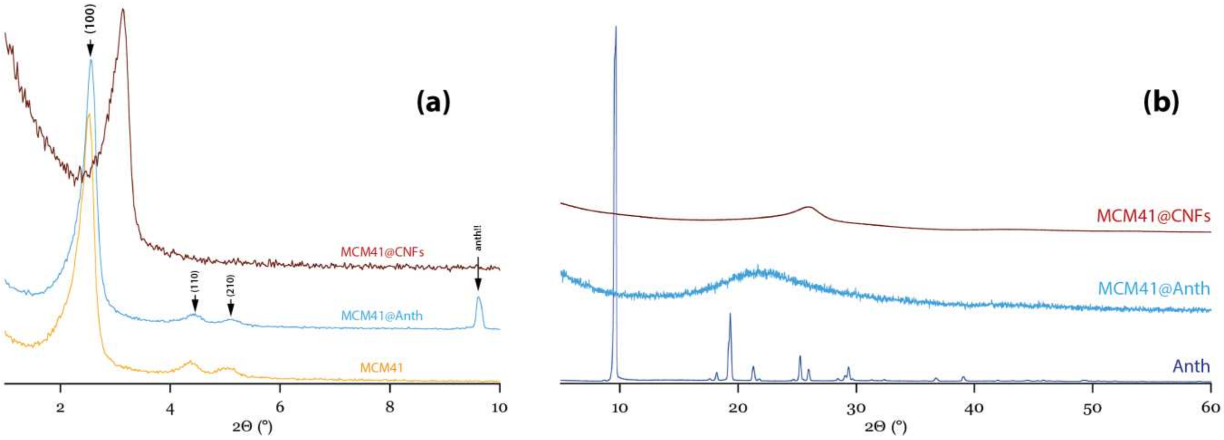

Figure 5. (a) XRPD of MCM-41 showing the low angle scattering regime ($2\theta < 10°$) of calcined MCM-41 (orange), MCM41@*anth* (light blue) and MCM41@CNFs (brown). (b) High angle area.

Synthesis of carbon nanoforms by confinement of anthracene in a mesoporous host.

CNFs were synthesized by following a three-step procedure (SI3). First, MCM-41 was loaded with *anth* by impregnation to yield MCM41@*anth*.[33] Dichloromethane was the solvent of choice due to its higher hydrophilicity over other standard organic solvents as the intrinsic hydrophobicity of *anth* might limit the filling of the pores. Next, MCM41@*anth* was transferred to a quartz tube, purged and sealed under vacuum. The tube was then subjected to a multiple-ramp thermal treatment (SI10), similar to that described above for the reaction of free *anth* molecules, followed by annealing in N_2 to produce MCM41@CNFs. Finally, the silica template was removed by etching with a diluted solution of hydrofluoric acid (HF).

XRPD. As illustrated in Fig.5a, the powder pattern of bare MCM-41 displays a strong diffraction peak and two weaker bands at low angles ($2\theta < 10°$) that can be indexed as (100), (110) and (210) by assuming a hexagonal cell. This gives a unit cell parameter a_o=3.45 nm, which stands for the center-to-center distance separating the 3D hexagonal array of cylindrical mesopores in the host. MCM41@*anth* is isostructural to MCM-41, confirming that the overall structure of the host is maintained after the loading of the guest. The poor scattering power of carbon does not allow for a preliminary estimate of the filling of the pores by analyzing the difference in the intensities of (100) reflections. This would be only valid for the loading of highly scattering materials like metals. In turn, MCM41@CNFs displays more drastic changes characterized by the broadening of (100), which also shifts to higher angles, and the weakening in intensity of (110) and (210). This change in the relative intensity of the peaks and the contraction of the lattice is generally observed when substituted MCM-41 is heated at high temperatures.[34-36] Comparison of the XRPD of the solid guest with

MCM41@*anth* at higher angles rules out the presence of co-precipitated aggregates of *anth* outside the pores (Fig.5b). After thermal treatment, MCM41@CNFs displays a broad signal centered at 26.6º (d=3.35 Å), reminiscent of that found for graphite,[29] suggesting the formation of graphitic-like materials within the pores of MCM-41.

Adsorption studies. Nitrogen adsorption/desorption experiments were used to confirm the intrinsic porosity of MCM-41 and confirm the loading of the pores with *anth*. Fig.6 shows the N_2 isotherm at 77 K of calcined MCM-41 and MCM41@anth. The host behaves as a mesoporous material, showing a type-IV isotherm according to the IUPAC classification. The gas uptake follows a linear increase at low pressures (P/P_0=0.05–0.25), due to the formation of a monolayer prior to filling of the pores. The BET surface area of 943 m^2 g^{-1}calculated from this linear region, is consistent with the values reported in the literature.[37] The shape of the isotherm is indicative of a narrow pore size distribution and the absence of a hysteresis loop confirms that the uptake of the gas is reversible and the pores become accessible once emptied. The BJH model provides a pore volume of 0.70 cm^3/g and a pore size of 2.22 nm. The amount of physisorbed N_2 decreases considerably for MCM41@*anth*. In fact, we can consider that the mesopores of the parent MCM-41 silica have been almost completely filled. This effect must be attributed to the loading of guest molecules inside the pores of MCM-41 that results in a drastic decrease of the surface area and pore volume down to 98 $m^2g^{-1}$and 0.08 cm^3/g, respectively. This surface area value mainly corresponds to the combination of external surface area and pore entrances with probably a low fraction of not completely filled mesopores. This is consistent with the BJH pore size distribution curve (SI4) that features a very low fraction of accessible porosity with a low intensity signal centered at 1.74 nm and two shoulders at *ca.* 1.89 and 2.11 nm.

Scanning Electron Microscopy (SEM). SEM images of MCM-41 and MCM41@*anth* (SI5) rule out the presence of residual aggregates of *anth* after impregnation. Both solids share equivalent morphologies and the loading of the guest takes place leaving the host undamaged.

TGA. MCM-41 displays high thermal stability with a very attenuated mass loss (1.83 %) upon heating the sample to 900 ºC under ambient conditions (Fig.7). This signal was used as a reference to estimate the amount of guest loaded in MCM41@*anth*. This last displays a gradual mass release of 3.65 % at around 300 ºC, which can be attributed to loaded *anth* in the sample (1.82 %). Interestingly, after the heat treatment the thermal stability in MCM41@G1 and MCM41@CNFs is increased up to 600 ºC where again a weight loss of 2.76 % is observed. This increased thermal stability must be assigned to the presence of graphitic-like species that have formed during the process. No clear differences in the thermal behavior are observed for the system before and after the annealing suggesting that the stability of the CNFs depends more on the spatial confinement rather than the nature of the species formed.

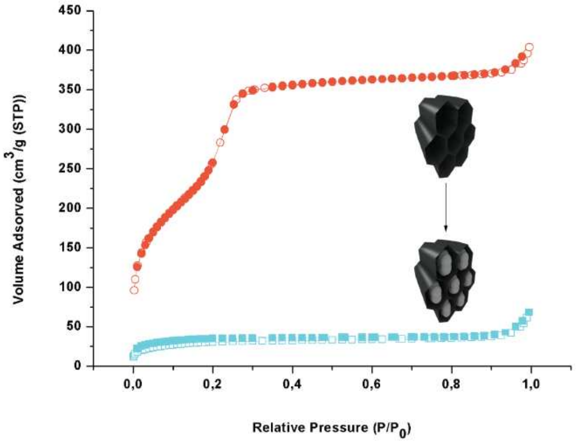

Figure 6. N_2 adsorption (*empty symbols*) / desorption (*filled synbols*) isotherms of calcined MCM-41 (*orange circles*) and MCM41@*anth* (*light blue squares*).

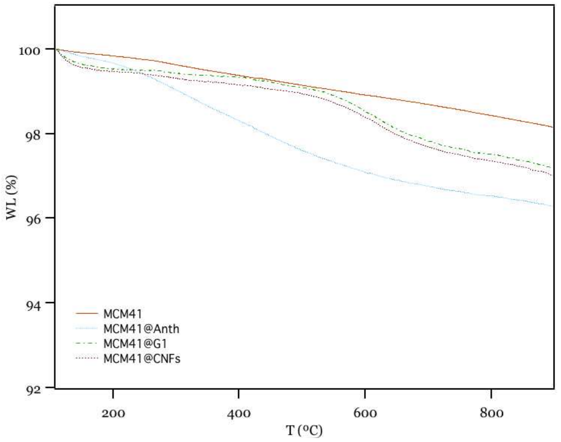

Figure 7. Thermogravimetry under ambient conditions of MCM-41 (orange, solid line), MCM@anth (light blue, dashed line), MCM41@G1 (light green, dotted line) and MCM41@CNFs (brown, dotted line).

Raman Spectroscopy. The spectrum of MCM41@G1 and MCM41@CNFs show the G and D bands characteristic of graphitic-like species (Fig.8). Albeit both solids display quite similar spectroscopic features, we will focus on the differences with the carbon product that results from the reaction of free *anth* molecules (G1). First, the broadening of D-bands is reduced for MCM41@G1 and MCM41@CNFs, suggesting less defective sp^2 carbon structure. The position of G shifts to higher wavenumbers over G1. Up-shifts of 5 cm^{-1} have been reported for the G-band in GNRs over bulk graphite due to confinement effects.[5] Here, the shift of the G-band by 9 and 11 cm^{-1} in MCM41@G1 and MCM41@CNFs, respectively, suggests the formation of CNFs of finite size. Next, the I_G/I_D ratio was used to estimate the relative size of the graphitic domains. The values summarized in Fig.8 indicate that the confinement of *anth* in the host yields CNFs with larger sp^2 domains. At this point is worth-noting that although the annealing of graphene promotes an increase in I_G/I_D, this is not the case for GNRs that generally display a constant ratio due to the weaker contribution of basal plane defects in comparison with the defects at the ribbon edges that activate the D-band.[38] This is also the case for our samples as I_G/I_D remains almost constant before (MCM41@G1) and after annealing (MCM41@CNFs).

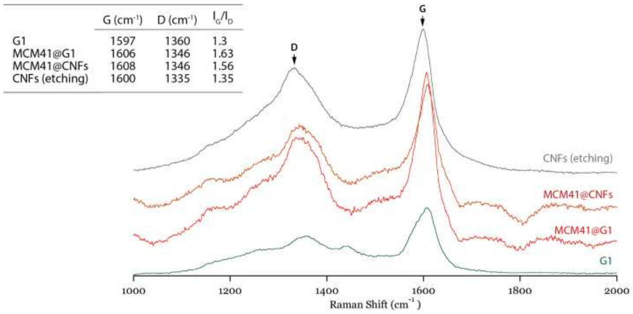

	G (cm^{-1})	D (cm^{-1})	I_G/I_D
G1	1597	1360	1.3
MCM41@G1	1606	1346	1.63
MCM41@CNFs	1608	1346	1.56
CNFs (etching)	1600	1335	1.35

Figure 8. μ-Raman spectra of G1 (green), MCM41@G1 (red), MCM41@CNFs (orange) and CNFs after partial etching with diluted HF (grey).

Finally, the Raman spectrum of the solid residue isolated by etching off the silica scaffold with HF, reveals some structural changes (Fig.8). G and D-bands red shift 8 and 11cm^{-1} with respect to MCM41@CNFs and the I_G/I_D ratio decreases to 1.35. This is indicative of a more defective material with reduced sp^2 domains and a carbon structure comparable to G1, suggesting that the CNFs are stabilized in the pores of MCM-41 and they collapse upon its removal.

HR-TEM. Images of the resultant solid residue after etching with HF provide valuable information on the morphology and structural characteristics of the isolated carbon nanoforms. First, the silica scaffold in MCM41@CNFs was removed by employing concentrated HF. As shown in Fig.9, the CNFs cannot be clearly observed by HR-TEM as they tend to aggregate and break into small pieces of 20-40 nm after removal of the template. This structural collapse is consistent with the Raman study above and is due to the close contact between the CNFs and the host. The removal of the silica induces a collapse of the CNFs that recalls the scenario recently described by Ogale *et al.* for a system containing G and SiO_2 nanoparticles.[39] Here, the authors report that HF treatment of the carbon/silica hybrid favors the introduction of holes to the resulting G lattice due to the close interaction between the silica and G. In order to stabilize the CNFs formed within the pores we decided to perform a partial etching of the silica scaffold by employing diluted HF. First, we removed partially the silica scaffold of MCM41@G1. However, this only yields an amorphous material (SI6). Thermal annealing favors the graphitization of the carbon matrix in MCM41@G1. Fig.10 and SI7 confirm that the product resulting from its etching is composed by elongated CNFs built from aggregation of up to 20 graphitic layers and carbon nanoonions (see last image in Fig.SI7) embedded in an amorphous silica matrix (SI8). This is remarkably different to that observed for G2 and suggests that the isolation of the PAHs inside the pores prevents their association by π-π intermolecular interactions and limits their arrangement to one direction thus enabling the growth of 1D CNFs. These show an average interlayer space of 0.34 nm that matches the separation between neighboring carbon layers in pristine graphite (*cf.* 0.35 nm). The medium average thickness of the obtained CNFs is around 3-4 nm confirming the templating role played by the pores of the MCM-41 host, which confine and direct the graphitization of the *anth* guests in 1D.

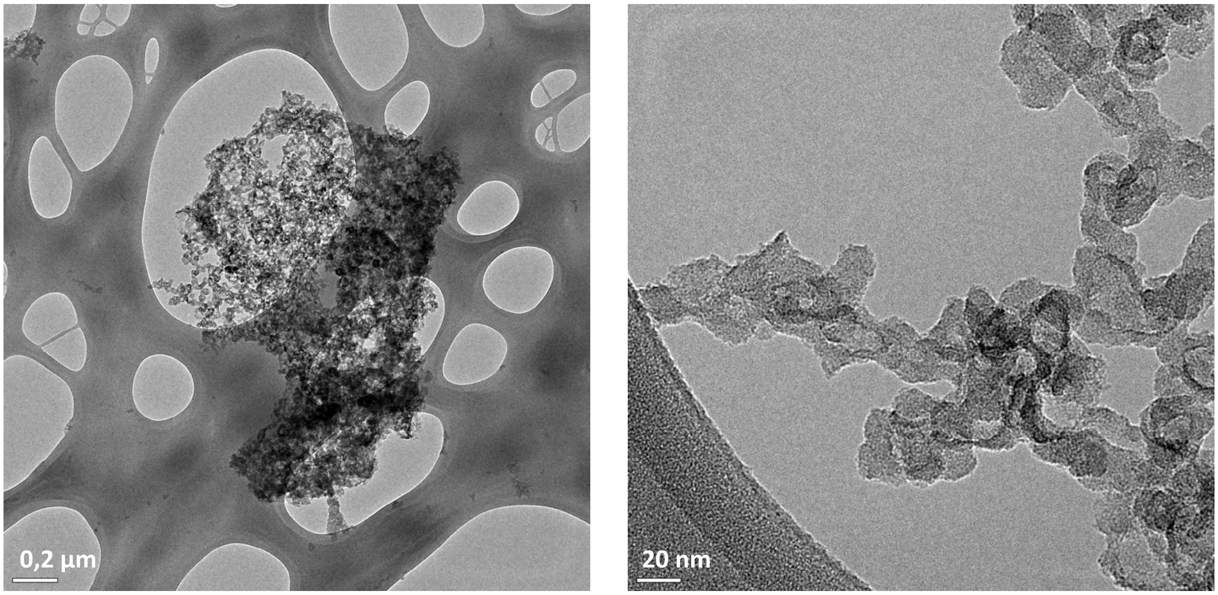

Figure 9. HR-TEM images of CNFs after etching of MCM41@CNFs with concentrated HF.

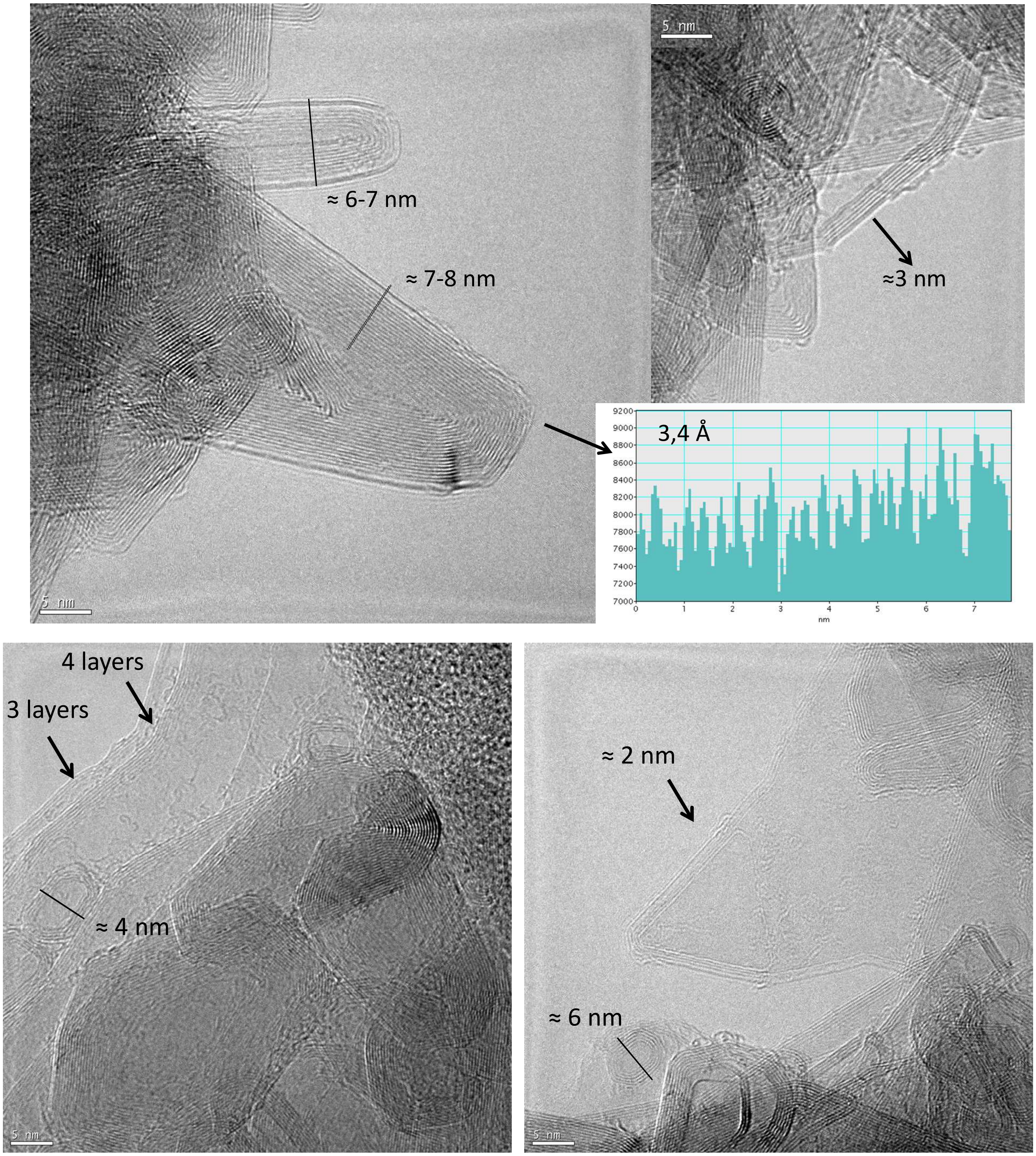

Figure 10. HR-TEM images of MCM41@CNFs after the etching with diluted HF. The images clearly show an increased graphitization, with the appearance of elongated CNFs displaying widths between 2-8 nm and closed CNFs with diameters of *ca.* 4-6 nm.

METHODS

General synthesis remarks. Graphite powder was purchased from Fisher Scientific (G/0900/60) and anthracene from Aldrich. The temperature conditions were obtained by employing a tubular furnace (Gallur). The dimensions of the quartz ampoule were 7 cm of length and diameter of 0.5 cm.

Synthesis of graphite (G2). Step 1: 2 g of anthracene were loaded inside a quartz ampoule, and sealed in vacuum. Afterwards, the quartz ampoule was place inside a furnace and the temperature raised to 520 ºC following the temperature gradient described in SI9. After the heat treatment a dark-brown solid appeared over the quartz tube walls (G1). Step 2: G1 was placed inside a tubular furnace purged with nitrogen. The temperature was set at 400 ºC and maintained during 4h under nitrogen atmosphere to produce G2 that was obtained as a black solid.

Synthesis of MCM-41. A solution of 2.61 g of silica, 8.4 g of tetramethylammonium hydroxide in 28 mL of deionized water was added to a polypropylene flask containing 13.21 g of Na_2SiO_4 in 62.16 mL of deionized water. Next, 9.66 g of additional silica were added to the mixture during 1 hour. A solution containing 31.2 g cetyltrimethyl ammonium bromide in 210 mL of water was carefully added to the mixture above and stirred during 1 hour. Next, the polypropylene flask was closed and heated in an oven up to 100 ºC during 4 days. Finally, MCM-41 was isolated by filtering the white powder formed and drying it at 100 ºC overnight.

Synthesis of carbon nanoforms (CNFs). Introduction of anthracene molecules within the pores of MCM-41 (MCM41@anth). Anthracene molecules were introduced into the pores of MCM-41 according to the impregnation method. 200 mg of MCM-41 (pre-calcined at 700 ºC during 10 hrs) were introduced inside a closed silica column. Next, 70 mg of anthracene dissolved in 10 mL of dichloromethane (CH_2Cl_2) were introduced inside the column, and the column was kept closed for 30 minutes. Finally, by applying pressure, the CH_2Cl_2 containing the non-introduced anthracene was quickly evacuated, followed by washing the sample with one additional milliliter of CH_2Cl_2. Finally, MCM41@anth was dried at 110 ºC during 2 hours.

Synthesis of CNFs. First, 150 mg of MCM41@anth were loaded inside a quartz ampoule and sealed in vacuum. The quartz ampoule was then place inside a furnace and the temperature raised to 520 ºC following the temperature gradient described in SI10 to produce MCM41@G1. In a second step, 100 mg MCM41@G1 were placed inside a tubular furnace purged with nitrogen. The temperature was set at 400ºC and maintained during 4h under nitrogen atmosphere to give MCM41@CNFs.

Etching with HF. To achieve a partial etching of the silica scaffold, a diluted solution of HF (0.1 mL HF in 1 mL of water) was employed directly over the sample. The black residue formed was washed thoroughly with water. WARNING: HF is very corrosive and it may cause severe burns, metabolic imbalances, pulmonary edema and life threatening cardiac arrhythmias. Even moderate exposures to concentrated HF may rapidly progress to fatality if left untreated. Handle HF just with plastic material, and clean carefully everything with high amounts of water.

Physical Characterization. IR spectrum was taken using FT-IR Nicolet 5700 spectrometer in the 4000-400 cm^{-1} frequency range, using powdered samples diluted in KBr pellets. HR-TEM images were obtained using a TECNAI G2 F20 microscope. Field Emission Gun (FEG)200 kV. Thermogravimetric analysis was carried out with a Mettler Toledo TGA/SDTA 851 apparatus in the 25-800^{o}C temperature range under ambient conditions. X-ray powder profile (XRPD) was collected using a Siemens D-500 X-ray difractometer (Cu-Kα radiation, $\lambda\alpha = 1.54184$ Å). Sample was grounded and mounted on a flat sample plate. Profile was collected as step scans in the $5º < 2\theta < 70º$ range with a spot size of 0.02º. Scanning electron microscopy (SEM) was performed in a Hitachi S-4800 microscope, having a resolution of 1.4 nm at 1kV. Surface area, pore size and volume values were calculated from nitrogen adsorption-desorption isotherms (-196°C) recorded on a Micromeritics ASAP-2020 automated analyzer. Samples were degassed for 12 hours at 110ºC and 10^{-6} Torr prior to analysis. Surface areas were estimated according to the BET model, and pore size dimensions were calculated by using the BJH model. μ-Raman measurements at room temperature were performed with a dispersive Jobin-Yvon LabRam HR 800 microscope, working with an excitation line of 532 nm. The scattered light was detected with a thermoelectric cooled (-70 ºC) charge coupled device detector (CCD). It also has an Olympus BXFM optic microscope. All the measurements were carried out directly over the sample. In the performed experiments, the power employed over the samples was of the order of 0.3 mW, and the exposition time 60 seconds.

CONCLUSIONS

Bulk graphite can be straightforwardly obtained from direct cyclodehydrogenation of anthracene molecules via a two-step procedure. This contrast with the use of coronene as polyaromatic hydrocarbons, which yields low-dimensional oligomers instead, probably due to the lower melting point of anthracene that reduces the kinetic energy necessary for the reaction to take place. Loading of anthracene inside the pores of the mesoporous MCM-41 prior to thermal treatment enables formation of graphitic CNFs. The confinement of the polyaromatic hydrocarbons to a constrained nanometric environment minimizes the π-π interactions between the aromatic core of the anthracene molecules, thus forbidding a 3D packing and favoring 1D-alignment of the anthracene molecules that promotes the formation of CNFs of a finite width limited by the porosity metrics of the host, rather than bulk graphite. Confinement also favors graphitization of the resulting carbon over that obtained by reaction of the unconfined material.

Our findings offer new opportunities to explore the role of chemically accessible hosts in templating nanocarbon growth. To date this is mainly limited to the synthesis of graphene nanoribbons by confinement inside CNTs.[16, 19, 24] Here the use of alternative mesoporous hosts like zeolites and, even more, the less robust but more chemically versatile Metal-Organic Frameworks (MOFs), represent and avenue worth being explored as they would offer a broader range of accessible pore sizes with variable connectivity and chemical functionality. Chemical modification of anthracene by introduction of peripheral substituents to gain control on its packing in the solid state through inter-molecular interactions and favor the efficiency of the cyclodehydrogenation reaction is currently undergoing.

ACKNOWLEDGEMENTS

Financial support from the EU (Projects HINTS and ERC Advanced Grant SPINMOL), the Spanish Ministerio de Economía y Competitividad (Projects MAT2011-22785), and the Generalitat Valenciana (Prometeo Program) are gratefully acknowledged. C.M.-G. thanks the Royal Society for a University Research Fellowship (UF120137).

Notes and references

[*,a] Prof. E. Coronado, Dr. C. Martí-Gastaldo, Dr. C. Bosch-Navarro, Universidad de Valencia (ICMol), Catedrático José Beltrán-2, 46980, Paterna (Spain).
[†] Current address: Department of Chemistry, University of Liverpool. Crown Street, L697ZD, Liverpool (UK).
[b] Prof. Pedro Amorós, Universidad de Valencia (ICMUV), Catedrático José Beltrán-2, 46980, Paterna (Spain)

Electronic Supplementary Information (ESI) available: [Synthetic details, SEM and additional HR-TEM images, FT-IR spectra, EDAX microanalysis and pore distribution of loaded MCM41@anth]. See DOI: 10.1039/b000000x/

1 J. Lu, I. Do, L.T. Drzal, R.M. Worden, I. Lee, *ACS Nano,* 2008, **2**, 1825.
2 a) C. Xu, X. Wang, J. Zhu, *Phys. Chem.* C, 2008, **112**, 19841. b) Y.C. Si, E.T. Samulski,. *Chem. Mater.,* 2008, **20**, 6792.
3 B. Luo, S. Liu, L. Zhi, *Small,* 2012, **8**, 630.
4 S. Park, R. S. Ruoff, *Nature Nanotech.,* 2009, **4**, 217.

5 C. N. R. Rao, A.K. Sood, K. S. Subrahmanyam, A. Govindaraj, *Angew. Chem. Int. Ed.,* 2009, **48**, 7752.

6 M. Inagaki, Y.A. Kim,. *J. Mater. Chem.,* 2011, **21**, 3280.

7 D. Wei, Y. Liu,. *Adv. Mater.,* 2010, **22**, 3225.

8 L. Zhi, K. Müllen,. *J. Mater. Chem.* 2008, **18**, 1472.

9 D. A. C. Brownson, C.E. Banks, *Phys. Chem. Chem. Phys.* 2012, **14**, 8264.

10 X. Wan, K. Chen, D. Liu, J. Chen, Q. Miao, J. Xu, *Adv. Mater.* 2012, **24**, 3906.

11 X. Yang, X. Dou, A. Rouhanipour, L. Zhi, H.J. Räder, K. Müllen,. *J. Am. Chem. Soc.* 2008, **130**, 4216.

12 J. Cai, P. Ruffieux, R. Jaafar, M. Bieri, T. Braun, S. Blankenburg, M. Muoth, A. P. Seitsonen, M. Saleh, X. Feng, K. Müllen, R. Fasel, *Nature,* 2010, **466**, 470.

13 M. Müller, V.S. Iyer, C. Kübel, V. Enkelmann, K. Müllen, *Angew. Chem. Int. Ed.,* 1997, **36**, 1607.

14 M. Treier, C.A. Pignedoli, T. Laino, R. Rieger, K. Müllen, D. Passerone, R. Fasel, *Nat. Chem.,* 2011, **3**, 61.

15 G. Abellán, E. Coronado, C. Martí-Gastaldo, A. Rivera, J. F. Sanchez-Royo, *Chem. Sci.* 2012, **3**, 1481.

16 G. Abellán, E. Coronado, C. Martí-Gastaldo, A. Rivera, T. F. Otero, *Part. Part. Syst. Charact.,* 2013, **30**, 853.

17 A. V. Talyzin, S. M. Luzan, K. Leifer, S. Akhtar, J. Fetzer, F. Cataldo, Y. O. Tsybin, C. W. Tai, A. Dzwilewski, E. Moons, *J. Phys. Chem. C,* 2011, **115**, 13207.

18 A. V. Talyzin, I. V. Anoshkin, A. V.; Krasheninnikov, R. M. Nieminen, A. G. Nasibulin, H. Jiang, E. I. Kauppinen, *Nano Lett.,* 2011, **11**, 4352.

19 J. Sun, H. Liu, D.G. Evans, W. Yang, X. Duan,. *Chem. Commun.,* 2012, **48**, 8126.

20 M. Fujihara, Y. Myata, R. Kitaura, Y. Nishimura, C. Camacho, S. Irle, Y. Iizumi, T. Okazaki, H. Shinohara, *J. Phys. Chem C,* 2012, **116**, 15141.

21 T. W. Chamberlain, J. Biskup, G. A. Rance, A. Chuvilin, T. J. Alexander, E. Bichoutskaia, U. Kaiser, A. N. Khlobystov, *ACS Nano,* 2012*,* **6**, 3943.

22 F. de Clippel, A. Harkiolakis, T. Vosch, X. Ke, L. Giebeler, S. Oswald, Houthoofd; J. Jammaer, G. Van Tendeloo, J.A. Martens, P. A.; Jacobs, G. V. Baron, B. F. Sels, J. F. M Denayer, *Microporous and mesoporous Materials* 2011, **144**, 120.

23 M. Clemente-Leon, E. Coronado, A. Forment-Aliaga, P. Amorós, J. Ramírez-Castellanos, J. M. González-Calbet, *J. Mater. Chem.,* 2003, **13**, 3089.

24 B. Tian, S. Che, Z. Liu, X. Liu, W. Fan, T. Tatsumi, O. Terasaki, D. Zhao, *Chem. Commun.* 2003, **21**, 2726.

25 M. Inagaki, H. Orikasa, T. Morishita,. *RSC Adv.,* 2011, **1**, 1620.

26 M. Ogawa, H. Shirai, K. Kuroda, C. Kato, *Clays and Clay Minerals* 1992, **40**, 485.

27 Y. Xhou, Q. Bao, L. A. L. Tang, Y. Zhong, K. P. Loh,. *Chem. Mater.* 2009, **21**, 2950.

28 C. Bosch-Navarro, E. Coronado, C. Marti-Gastaldo, J. F. Sánchez-Royo, M. Gomez-Gomez, *Nanoscale,* 2012, **4**, 3977.

29 G. Eda, M. Chhowalla, *Adv. Mater.,* 2010, **22**, 2392.

30 C. Castiglioni, C. Mapelli, F. Negri, G. Zerbi, *J. Chem. Phys.* 2001, **114**, 963.

31 K. N. Kudin, B. Ozbas, H.C. Schniepp, R.K. Prud'homme, I. A. Aksay, R. Car, *Nano Lett.*, 2008, **8**, 36.

32 C. Charnay, S. Begu, C. Tourne-Peteilh, L. Nicole, D.A. Lerner, J.M. Devoisselle,. *Eur. J. Pharm. Biopharm.,* 2004, **57**, 533.

33 J. Yu, Z. Feng, L. Xu, M. Li, Q. Xin, Z. Liu, C. Li, *Chem. Mater.* 2001, **13**, 994.

34 T. Abdel-Fattah, *Fuller. Nanotub. Carbon. Nanostruct.,* 2006, **14**, 585.

35 G. D. Mihai, V. Meynen, M. Mertens, N. Bilba, P. Cool, E. F. Vansant, *J. Mater. Sci.,* 2010, **45**, 5786.

36 C. P. Jaroniec, M. Kruk, M. Jaroniec,. *J. Phys. Chem. B,* 1998, **102**, 5503.

37 S. Ryu, J. Maultzsch, M. Y. Han, P. Kim, L. E. Brus, *ACS Nano,* 2011, **5**, 4123.

38 D. Mhamane, W. Suryawanshi, S. M. Unni, C. Rode, S. Kurungot, S. Ogale, *Small,* 2013, **9**, 2801.

One-dimensional carbon nanoforms are preferentially obtained by fusion of anthracene molecules in the pores of a mesoporous MCM-41 host.